

Journal of Materials Chemistry B

Accepted Manuscript



This is an *Accepted Manuscript*, which has been through the Royal Society of Chemistry peer review process and has been accepted for publication.

Accepted Manuscripts are published online shortly after acceptance, before technical editing, formatting and proof reading. Using this free service, authors can make their results available to the community, in citable form, before we publish the edited article. We will replace this *Accepted Manuscript* with the edited and formatted *Advance Article* as soon as it is available.

You can find more information about *Accepted Manuscripts* in the [Information for Authors](#).

Please note that technical editing may introduce minor changes to the text and/or graphics, which may alter content. The journal's standard [Terms & Conditions](#) and the [Ethical guidelines](#) still apply. In no event shall the Royal Society of Chemistry be held responsible for any errors or omissions in this *Accepted Manuscript* or any consequences arising from the use of any information it contains.



Differential sub-cellular processing of single-wall carbon nanotubes via interfacial modifications

Brian D. Holt,^a Kris Noel Dahl,^{b,c,*} and Mohammad F. Islam^{a,*}

Received 00th January 20xx,
Accepted 00th January 20xx

DOI: 10.1039/x0xx00000x

www.rsc.org/

Strategies for cell-specific targeting and delivery of carbon nanotubes have made significant advancements over recent years. However, control of sub-cellular localization, an important criterion for many biomedical applications, remains largely unexplored. In this work, we experimentally demonstrate how different molecules that are used to non-covalently suspend hydrophobic SWCNTs in aqueous conditions also influence cellular processing and localization. We utilized complementary imaging modalities to show that SWCNTs dispersed using the membrane active tri-block copolymer Pluronic® F-127 (PF127) were endocytosed into cells by the millions but eventually escaped endosomes and altered F-actin structures. In contrast, SWCNTs dispersed with the protein bovine serum albumin (BSA) were endocytosed into cells at similarly high levels but remained in the endosomal pathway, ultimately co-registering with endoplasmic reticulum and vesicles. Interestingly, cellular exposure to SWCNTs–BSA in the presence of the endosome disrupter, chloroquine, led to altered F-actin structures that were similar to the alterations induced by cellular exposure to SWCNTs–PF127. These results suggest that PF127 facilitated endosome escape and that SWCNTs might have an energetically favorable interaction with stiff, filamentous structures inside the cell. Thus, our results provide a design principle for non-covalent surface modifications of SWCNTs that do not degrade the desirable, intrinsic SWCNT properties but provide differential trafficking to intracellular compartments for sub-cellular biomedical applications.

Introduction

The development of nanomaterials for cellular delivery has been the focus of significant research efforts in recent years to advance their utilization in biomedical applications. Single wall carbon nanotubes (SWCNTs), for example, have been modified covalently^{1,2} and non-covalently^{2,3} for targeting to specific cells due to their small size and high surface area that allow for multi-functionalization. Also, bare SWCNTs are hydrophobic and require surface modification to prevent aggregation into bundles⁴ that are deleterious to cells.⁵⁻⁹ Covalent attachment of small molecules to SWCNTs has yielded excellent individually dispersed SWCNTs that enter cells and are nontoxic.^{1,2} However, covalent alterations destroy the desirable thermal, electrical, mechanical and optical properties of individualized SWCNTs.¹⁰ Surfactants from the cholate¹¹ and sulfonate¹² families are highly efficacious at non-covalently dispersing SWCNTs, but these classes of surfactants are toxic to cells.^{13,14} Recently, our group^{9,15,16} and many others¹⁷⁻²⁶

have developed biologically relevant SWCNT dispersions using non-covalently linked block copolymers such as Pluronic® F-127 (PF127), biomolecules such as DNA and proteins, including bovine serum albumin (BSA), γ -globulin, *etc.*, and combinations such as polymers grafted onto polydopamine.

The interfacial properties as well as the shape, size and surface charge of engineered nanomaterials, including polymeric nanoparticles, liposomes, quantum dots, noble metal nanoparticles, silica-based nanoparticles, poly(lactic-co-glycolic acid) nanoparticles, *etc.*, have been manipulated to alter cellular internalization pathways which can, in turn, alter sub-cellular localization.²⁷ Such approaches for controlling sub-cellular distribution of nanoparticles, particularly interfacial modification based methodologies, have been extended to SWCNTs to guide SWCNTs to specific sub-cellular regions including the membrane,²⁸⁻³¹ nucleus³²⁻³⁵ and mitochondria.³⁶⁻⁴⁰ For instance, it has been demonstrated that SWCNTs could be localized to the cell nucleus by covalently modifying nanotubes with fluorescein isothiocyanate-labeled poly(ethylene glycol).³³ Others have employed numerous, diverse covalent modifications of SWCNTs to localize nanotubes within peri-nuclear sub-cellular regions.⁴¹ However, delivery of SWCNTs to sub-cellular compartments while maintaining the intrinsic, desirable properties of SWCNTs has thus far attracted relatively limited effort and/or success.

Here, we explore the influence of non-covalently attached dispersing agents on the sub-cellular trafficking and localization of highly purified, short and length selected (145 ±

^a Department of Materials Science and Engineering, Carnegie Mellon University, 5000 Forbes Avenue, Pittsburgh, Pennsylvania 15213-3815, USA. E-mail: mohammad@cmu.edu

^b Department of Biomedical Engineering, Carnegie Mellon University, 5000 Forbes Avenue, Pittsburgh, Pennsylvania 15213-3815, USA. Email: krisdahl@cmu.edu

^c Department of Chemical Engineering, Carnegie Mellon University, 5000 Forbes Avenue, Pittsburgh, Pennsylvania 15213-3815, USA.

† Electronic Supplementary Information (ESI) available: [details of any supplementary information available should be included here]. See DOI: 10.1039/x0xx00000x

17 nm) SWCNTs⁹ within the cell. We have previously characterized dispersions of this type of SWCNT with polymers, such as PF127, and proteins, such as BSA, and demonstrated that these well-dispersed SWCNTs rapidly enter cells at high levels (millions of SWCNTs with a total mass on the order of pg per cell)^{15,42,43} without inducing toxicity to cells.^{9,42,43} Real-space fluorescence imaging of cellular compartments and SWCNTs and confocal Raman imaging of SWCNTs showed that SWCNTs dispersed with the protein BSA remained in the metabolic pathway: SWCNTs–BSA were retained in endosomes and co-registered with endoplasmic reticulum (ER) and vesicles. In contrast, SWCNTs dispersed with the polymer PF127 escaped endosomes and co-localized with apical filamentous-actin (F-actin) structures. To quantify these differential sub-cellular interactions, we imaged the localization of SWCNTs in real-space using fluorescence and Raman imaging, determined interactions between SWCNTs and various sub-cellular structures including F-actin and endosomes using fluorescence lifetime imaging microscopy (FLIM), and visualized cellular compartmental redistribution caused by SWCNTs using confocal fluorescence microscopy. Our results suggest that the dispersing agent of SWCNTs could be designed to preferentially traffic SWCNTs to different sub-cellular compartments, allowing for further advancement of sub-cellular targeting for biomedical applications.

Experimental

Preparation and characterization SWCNT dispersions

Uncoated SWCNTs are hydrophobic and bundle in an aqueous environment due to an interaction energy of $\sim 40 k_B T/nm$.⁴ Bundling suppresses the desirable properties of SWCNTs,⁴⁴ and SWCNT bundles can induce toxicity in cells.⁵⁻⁸ Dispersion of SWCNTs using sonication in the presence of a dispersing agent results in a suspension that contains individualized SWCNTs as well as small and large bundles of SWCNTs.⁴⁵ Centrifugation can remove most if not all of the large and small bundles with individualized SWCNTs remaining in the supernatant.⁴⁴⁻⁴⁷ The presence of highly resolved van Hove peaks in absorbance and fluorescence spectra are typically taken to be an indication that the SWCNT dispersion contains individualized SWCNTs.⁴⁵⁻⁵¹

SWCNTs used in this study were the same as those used by our group previously.^{9,15,16,31,42,43,52} Briefly, raw HiPCO (high-pressure carbon monoxide synthesis) SWCNTs (Unidym) were purified^{9,53,54} and length fractionated^{9,55-57} as previously reported⁹ to remove carbonaceous impurities and toxic metal catalysts and to generate a sample with a narrow length distribution. The final material contained <5 wt.% carbonaceous and $\sim 0.3\%$ metallic impurities and the SWCNTs had a length distribution of 145 ± 17 nm.⁹

SWCNTs were dispersed as previously described.^{9,15} Briefly, SWCNTs were dispersed at 0.1 wt.% in ultrapure water by probe-tip sonication (Fisher Scientific, Sonic Dismembrator Model 100, 3 mm probe tip) for 2 h at 6 W with either PF127 (BASF) or BSA (Sigma-Aldrich) at a SWCNT to dispersing agent weight ratio of 1:10. Note that for these sonication parameters, SWCNTs of ~ 145 nm in length are considered to not undergo any sonication-induced scission.⁵⁸ SWCNTs–PF127 were centrifuged for 30 min⁹ and SWCNTs–BSA were centrifuged for 7 min¹⁵ at $21,000\times g$ to separate individual SWCNTs that stayed in the supernatant from small and large

bundles of SWCNTs that transferred to the sediment. Supernatants were collected and subjected to optical characterization *via* UV–vis–NIR (near-infrared) absorbance spectroscopy (Varian Cary 5000 UV–vis–NIR spectrophotometer) and Raman spectroscopy (inVia confocal Raman microscope, Renishaw) (Fig. S1). NIR fluorescence spectroscopy of SWCNTs is reported elsewhere^{9,15,42} and confirmed the presence of individualized SWCNTs.⁴⁵ The concentration of SWCNTs was determined using an absorbance coefficient of 2.6 (absorbance mL) / (mm mg) at 930 nm.^{9,16,57} Note that the reported concentrations of SWCNT dispersions indicate the mass of SWCNTs and do not include the mass of the associated dispersing agent. Supernatants were sterilized *via* UV lamp for 1 h prior to cellular experiments.

Cell culture, transfections, and chemical treatments

Cell culture. HeLa cells were chosen due to their passage-to-passage consistency, ease of transfection and lack of phagocytosis (*i.e.*, they will only undergo endocytosis of material). HeLa cells (ATCC CCL2) were cultured in complete cell culture media as per ATCC recommendations: Dulbecco's Modified Eagle Medium (Thermo Scientific Hyclone), 10% v/v fetal bovine serum (Invitrogen) and 1% v/v penicillin–streptomycin (Invitrogen) at 37 °C and 5% CO₂. Cells were seeded onto sterilized, #1.5 coverslips in 35 mm dishes at 3.0×10^4 cells/cm²; after 24 h cells were exposed to SWCNTs. SWCNTs were diluted to their final concentration in complete cell culture media, and additional fetal bovine serum was added to ensure that the final media fetal bovine serum concentration remained at 10% v/v. Dispersing agent controls were 1 wt.% BSA or 1 wt.% PF127 solutions that were added to the cell culture media at the same volume as that added for the exposure to SWCNTs–BSA or SWCNTs–PF127, respectively. SWCNT exposure times and concentrations are indicated for each experiment but were typically 24 h and 50 μ g/mL, respectively.

Transfection. For transient transfection, HeLa cells were grown to ~ 40 – 60% confluency and then transfected using Polyfect (Qiagen) with one of three plasmids according to manufacturer's recommendations. Three different plasmids were used for transfection: pCS107-GFP-moe (GFP-moesin, which labels but does not alter F-actin structures⁵⁹), pAc-GFP1-Endo (GFP-RhoB GTPase that labels endosomes, Clontech) or pEGFP-C1 (GFP with no target gene allowing for production of GFP with non-specific localization to the cytoplasm, Clontech). 24 h after transfection, the media was changed, and SWCNTs were added as indicated for each experiment for the indicated exposure time. Finally, the cells were washed, fixed and mounted for imaging.

Fluorescent labels. When indicated, the cell-permeable, nucleic acid fluorophore Hoechst 33342 (Invitrogen) was exposed at 10 μ g/mL to live cells for 15 min to label nuclei. After fixation, as indicated, cells were permeabilized with 0.2 wt.% Triton X-100 for 3 min and then washed with phosphate buffered saline. To primarily label ER and vesicles, the fixed and permeabilized cells were exposed to 25 μ M of the lipophilic styryl dye FM® 4-64 (Life Technologies) for 30 min. To label the DNA of nuclei, the fixed and permeabilized cells were exposed to 4',6-diamidino-2-phenylindole, dihydrochloride (DAPI, Life Technologies) at 0.25 μ g/mL for 30 min. To label F-actin, the fixed and permeabilized cells were exposed to Oregon Green® 488 phalloidin (Life Technologies) at 0.165 μ M for 30 min. Finally, the cells were washed 3 \times with PBS before mounting onto glass microscopy slides in the presence of Fluoromount-G (SouthernBiotech).

Chloroquine treatment. Chloroquine diphosphate salt (chloroquine, Sigma-Aldrich) treatment was applied to cells in a

manner similar to a previously reported protocol.⁶⁰ HeLa cells were cultured and seeded as indicated above. After 24 h, the media was exchanged, and the cells were exposed to sterile filtered chloroquine diluted to 200 μM in cell culture media with experimental conditions added as indicated. The cells were incubated for 4 h and then were either immediately fixed (0 h post exposure) or had the media exchanged for fresh, complete cell culture media for 15 h and then fixed (15 h post exposure).

Optical imaging and analysis

Widefield imaging. Widefield phase contrast and fluorescence imaging was performed on a Leica DMI 4000B with a condenser with 0.9 numerical aperture (NA) and either a 40 \times with 1.2 NA or 100 \times with 1.4 NA oil immersion objective.

Confocal imaging. Confocal fluorescence imaging was performed on a Leica TCS SP5 inverted laser scanning confocal microscope with a 100 \times with 1.4 NA oil immersion objective. Series of confocal images acquired along the vertical direction (*i.e.*, Z-stacks) were acquired with ~ 100 nm step size, 1024 pixels \times 1024 pixels, ≥ 4 frame averaging and a scan rate of 700 Hz. Compressions of these three dimensional stacks were performed in Leica Advanced Fluorescence software.

Raman imaging. SWCNTs possess unique, intense Raman scattering,^{61,62} and their G-band can be used to image and quantify local SWCNT concentration.^{15,42,43,63,64} Therefore, we acquired maps of Raman spectra of cells exposed to SWCNTs and quantified the G-band intensity of SWCNTs to image the sub-cellular localization of SWCNTs. We used a confocal Raman microscope (inVia, Renishaw) with a 100 \times with 1.4 NA phase contrast oil immersion objective. Phase contrast images of the cells were acquired, and then Raman mapping was performed over those cells. Typical mapping experiments were performed with an X–Y step size of 1 μm , a laser power of ~ 5 mW at the sample and an integration time of 1.5 s. Spectra were acquired between 1188 and 1695 cm^{-1} with a resolution of ~ 1 cm^{-1} . Quantification of the intensity of the G-band at ~ 1591 cm^{-1} and the generation of heat maps of SWCNTs were performed using in-house code written in MATLAB[®] (The Mathworks, Inc.). To co-register heat maps of the G-band intensity of SWCNTs to fluorescence images of cellular compartments, the same fields of view were imaged with the Raman microscope and a separate fluorescence microscope, using phase contrast images to align the co-registration of the images.

SWCNT NIR fluorescence imaging. Individually dispersed, semi-conducting SWCNTs possess NIR fluorescence.^{45,50} We utilized the NIR fluorescence of SWCNTs to image the sub-cellular localization of SWCNTs using a custom microscope. Our excitation beam path included a 785 nm fiber-coupled, collimated laser excitation (120 mW 785 nm laser, Crystalaser); a custom, zero-order quarter-wave plate for 785 nm to circularly polarize the laser (Thorlabs, Inc.); an “engineered diffuser” (ED1-C20, Thorlabs, Inc.) to reduce coherence and uniformly expand the beam; and a bi-convex lens to collect and collimate the beam before entry into the microscope optical train (Leica DMI 4000B). Within the microscope, we used a custom NIR filter cube (Semrock): a 785 nm notch excitation filter, a 790 nm dichromatic mirror and a 792 nm long-pass emission filter. To further filter the light before reaching the detector, we included a 900 nm long-pass filter (Thorlabs, Inc.) in the emission path after the filter cube before the detector. To maximize detection of the NIR fluorescence of SWCNTs, we used a liquid-nitrogen cooled, highly sensitive, InGaAs focal plane array detector (2D-OMA V, Princeton Instruments).

Fluorescence lifetime imaging. FLIM was performed as previously described by our group^{31,52} using a tunable, mode-locked Ti:sapphire pulsed laser at 942 nm (Chameleon, Coherent) and a time-correlated single photon counting (TCSPC) board (Becker & Hickl SPC-830). For TCSPC, DCC software controlled the hardware, SPCM software acquired lifetime images and SPCImage software (Becker & Hickl) was used to calculate the fluorescence lifetime fits per pixel, generate lifetime images and export the pixel-by-pixel lifetime data for further aggregate analysis. To maximize accuracy and minimize the coefficient of variation of the lifetime, 220 time channels with a measurement window of 10.8 ns were used, and scans lasted at least 180 s for images of 256 pixels \times 256 pixels.^{65–67}

Image Processing and Statistical analysis. FLIM images were peak intensity thresholded in SPCImage to exclude background pixels from analysis. The corresponding fluorescence intensity images were also thresholded in ImageJ (National Institutes of Health) to exclude any pixels that were extracellular or only represented autofluorescence and not fluorescence of GFP (Fig. S2). Both thresholding procedures were used to threshold the final lifetime images and quantitative results. Thresholded lifetime data was analyzed in MATLAB[®] using previously developed in-house code to quantitatively determine the average, standard deviation, and distribution of fluorescence lifetime and goodness of fit (χ^2) on a per image basis, along with applying the thresholding based on the images of fluorescence intensity.^{31,52}

Fluorescence lifetime is quantitatively modeled as a sum of exponential decays:^{65,68}

$$I(t) = I_0 + \sum_i a_i e^{-t/\tau_i} \quad (1)$$

where $I(t)$ is the number of emitted photons as a function of time, a_i is the i^{th} relative amplitude of the i^{th} exponential and τ_i is the lifetime of the i^{th} exponential. For all FLIM images, the χ^2 of both a single ($i = 1$) and a double ($i = 2$) exponential decay was calculated, and for all images a double exponential model best represented the data. For multi-exponential fits, τ_m was used to characterize the fluorescence lifetime as a single parameter:

$$\tau_m = \sum_i a_i \tau_i / \sum_i a_i \quad (2)$$

and explicitly for $i = 2$

$$\tau_m = (a_1 \tau_1 + a_2 \tau_2) / (a_1 + a_2) \quad (3)$$

Final quantitative results are an aggregation of multiple fields of view, and note that each included (*i.e.*, non-thresholded) pixel of a FLIM image represents an individual data point.

Confocal X–Z images (Z-stacks compressed in Y) were analyzed in MATLAB[®] using in-house code. Average intensity per pixel along the X-direction was normalized to 0 – 1 in the Z-direction, based on where both apically and basally the image reached 10% of its maximum normalized Z-slice average intensity per pixel. Typically, final data represent the averaging of multiple fields of view together; hence, the aggregate intensity plots may not reach a value of 1 since the maximum average intensity per pixel may occur at different normalized Z-positions. When indicated, the plots were shifted to align the peak intensities with the peak intensity of control.

Statistical analysis was performed using a two-sample t-test for comparison of means of continuous data and a two-sample proportion Z-test for comparison of proportions (*e.g.*, multi-nucleation data). Differences were considered significant if $p < 0.05$. To minimize Type I error, a Bonferroni Correction was applied to data sets of which > 5 hypotheses were statistically tested.

Results and discussion

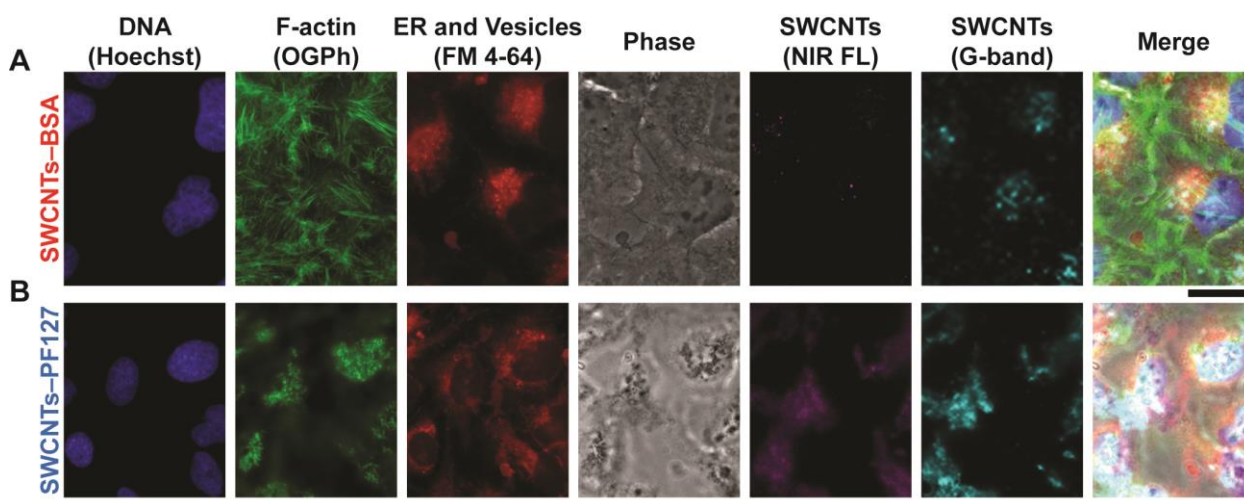


Fig. 1 Real-space imaging of the sub-cellular localization of SWCNTs prepared with different dispersing agents. HeLa cells were exposed for 24 h to 50 $\mu\text{g}/\text{mL}$ of (A) SWCNTs–BSA or (B) SWCNTs–PF127. SWCNTs–BSA primarily co-registered with ER and vesicles while SWCNTs–PF127 primarily co-registered with apical F-actin. At least 10 cells were imaged in each experiment. Scale bar is 20 μm .

Sub-cellular localization of SWCNTs *via* real-space imaging

To determine the sub-cellular localization of SWCNTs as a function of dispersing agent, we imaged SWCNTs and co-registered the signal with fluorescently labeled cellular compartments (Fig. 1). Individually dispersed, semi-conducting SWCNTs inherently possess NIR fluorescence,^{45,50} allowing for fluorescence-based imaging using a custom-built microscope.^{47,69-72} The unique Raman signatures of SWCNTs also enabled imaging of the spatial distribution of SWCNTs.^{61,63,73-75} In this work, we performed widefield NIR fluorescence and Raman imaging of the same fields of view to accurately determine SWCNT sub-cellular localization.

Real-space widefield imaging of HeLa cells exposed to 50 $\mu\text{g}/\text{mL}$ of SWCNTs–BSA showed peri-nuclear sub-cellular localization of SWCNTs–BSA (Fig. 1A). Visually, SWCNTs–BSA primarily co-registered with ER and vesicles but not with F-actin or DNA. To quantify the degree of co-localization of SWCNTs with cellular compartments, we calculated the two-dimensional correlation coefficient between images of SWCNTs that were obtained *via* Raman imaging using the G-band of SWCNTs and images of the fluorescently labeled cellular compartments. The two-dimensional correlation coefficient for SWCNTs–BSA and ER and vesicles was 0.61 compared to only 0.07 for SWCNTs–BSA and F-actin. In contrast, SWCNTs–PF127 manifested a different sub-cellular localization (Fig. 1B). Upon focusing the high-resolution widefield microscope on the apical regions of the cells, intense F-actin fluorescence was detected along with NIR fluorescence from SWCNTs–PF127. Raman G-band signal, acquired in “standard” mode, from SWCNTs–PF127 visually co-registered with apical F-actin structures but not with other cellular compartments, including basal F-actin (Fig. S3). The two-dimensional correlation coefficient for the images of the G-band of SWCNTs–PF127 and apical F-actin was 0.39 but was only 0.02 for SWCNTs–PF127 and basal ER and vesicles.

Sub-cellular interactions by FLIM

Fluorescence lifetime is related to the period of time between excitation of and emission from a fluorophore.⁶⁸ It is essentially independent of excitation energy and fluorophore concentration but is highly sensitive to the environment within ~ 5 nm surrounding the fluorophore.⁶⁸ This high environmental sensitivity of

fluorescence lifetime can be exploited to determine the presence of external quenching molecules in the near vicinity of the fluorophore.⁶⁸ We have previously shown a dramatic change of fluorescence lifetime of different fluorophores in the presence of SWCNTs including rhodamine, CellMask™ Orange, Oregon Green® 488 and green fluorescent protein (GFP).^{31,52} Here, we utilized changes in fluorescence lifetime associated with the GFP tagged to proteins in different cellular compartments to identify co-localization with SWCNTs. We transfected HeLa cells with GFP-RhoB GTPase to label endosomes, GFP-moesin to label F-actin or GFP to label cytoplasm. By using GFP for all of the cellular compartment fluorophores, we were able to more directly compare the interactions between SWCNTs and intra-cellular structures and avoided complications that could have arisen from probe-specific quenching levels of fluorescence lifetime.

Co-localization of SWCNTs–PF127 with apical F-actin. GFP-moesin, which binds to F-actin without altering structures,⁵⁹ showed well-defined F-actin structures for control HeLa cells. The mean fluorescence lifetime (τ_m , see Experimental Section) of GFP-moesin in control cells was uniform throughout the cell, but τ_m was heterogeneous and reduced in HeLa cells that were exposed to either 50 $\mu\text{g}/\text{mL}$ of SWCNTs–PF127 or SWCNTs–BSA for 24 h (Fig. 2A).

Histograms of τ_m of GFP-moesin show redistribution associated with SWCNT exposure (Fig. 2B). For control cells, 99% of the τ_m of GFP-moesin was within 2.00–2.40 ns. Cellular exposure to SWCNTs–PF127 caused a severe quenching of τ_m , as only 23% of τ_m was within the primary range for control cells (2.00–2.40 ns) while 19% was highly quenched (0–0.40 ns). In contrast, the quenching of the τ_m of GFP-moesin by SWCNTs–BSA was more moderate as only 5% was highly quenched (0–0.40 ns), and the average τ_m was 110% less quenched than that for cells exposed to SWCNTs–PF127. As a control, we examined the change in the average τ_m of GFP that remained soluble in the cytoplasm. The average τ_m of GFP for cells exposed to SWCNTs–PF127 was statistically similar to that of cells exposed to SWCNTs–BSA (Fig. S4C). These FLIM results further corroborate the real-space imaging results that showed that SWCNTs–PF127 but not SWCNTs–BSA co-registered with apical F-actin structures.

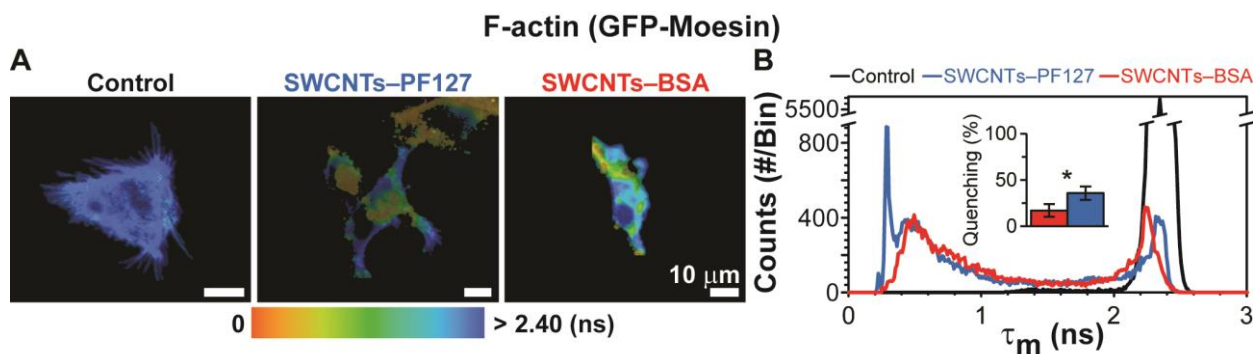


Fig. 2 FLIM of GFP-moesin that labeled F-actin in HeLa cells exposed for 24 h to 50 $\mu\text{g}/\text{mL}$ of SWCNTs stabilized with different dispersing agents. (A) Heat map images of the τ_m of GFP-moesin. Note that each pixel represents an individual data point of τ_m . (B) Histogram of the τ_m of GFP-moesin from all FLIM images. The inset is the percent quenching of the average τ_m compared to control. The total number of τ_m data points is > 30,000 for each experimental condition.

Co-localization of SWCNTs-BSA with endosomes. We examined the co-localization of SWCNTs with endosomes by performing FLIM of HeLa cells that were transfected with GFP-RhoB GTPase that labeled endosomes. Control HeLa cells displayed numerous observable endosomes throughout the cell. However, after 24 h of cellular exposure to 50 $\mu\text{g}/\text{mL}$ of either SWCNTs-PF127 or SWCNTs-BSA, the fluorescence of GFP-RhoB GTPase that labeled endosomes was less intense and the average τ_m was substantially reduced (Fig. 3A).

To visualize the distribution of the τ_m of GFP-RhoB GTPase that labeled endosomes, we generated a histogram of τ_m from the pixels of all the FLIM images (Fig. 3B). For control cells, 74% of the τ_m of GFP-RhoB GTPase was within 2.00–2.40 ns. The average τ_m of GFP-RhoB GTPase was dramatically quenched for cells that were exposed to SWCNTs-BSA for 24 h, as only 4% was within the primary range for control cells (2.00–2.40 ns) and 27% was highly quenched (0–0.40 ns). In contrast, cellular exposure to SWCNTs-PF127 resulted in less quenching, as 18% remained within the control range (2.00–2.40 ns) and only 11% was highly quenched (0–

0.40 ns). Comparatively, cellular exposure to SWCNTs-BSA resulted in a 40% greater reduction in the average τ_m than that of cells exposed to SWCNTs-PF127. We interpret this significantly greater level of quenching of the average τ_m of GFP-RhoB GTPase that labeled endosomes for cells exposed for 24 h to SWCNTs-BSA compared to cells exposed to SWCNTs-PF127 to indicate that SWCNTs-BSA remained in the endocytic pathway.

Collectively, we considered the FLIM data of the quenching associated with GFP-moesin, GFP-RhoB GTPase and GFP as a map of the sub-cellular localization of SWCNTs. To determine how the dispersing agent affected the trafficking of SWCNTs for short exposure times, we quantified the quenching of the average τ_m of GFP-moesin, GFP-RhoB GTPase and GFP as a function of exposure time up to 25 min. For exposure durations up to 25 min, both SWCNTs-PF127 and SWCNTs-BSA did not significantly alter the average τ_m compared to control (Fig. S4). The minimal quenching of the average τ_m of the GFP-labeled cellular compartments suggested that although cellular association of SWCNTs is rapid,^{42,70,76} SWCNT sub-cellular trafficking is a slower process.

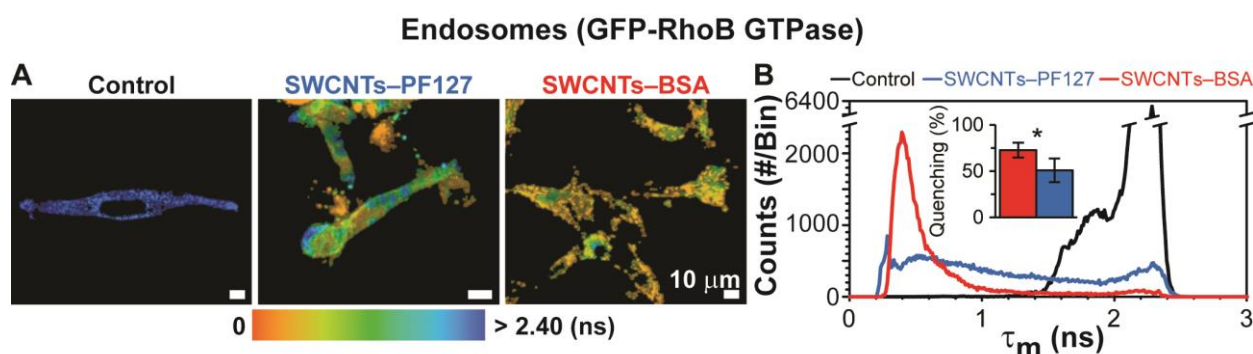


Fig. 3 FLIM of GFP-RhoB GTPase, which labeled endosomes, in HeLa cells exposed for 24 h to 50 $\mu\text{g}/\text{mL}$ SWCNTs stabilized with different dispersing agents. (A) Heat map images of τ_m of GFP-RhoB GTPase. (B) Histogram of the τ_m of GFP-RhoB GTPase from all FLIM images. The inset is the percent quenching of the average τ_m compared to control. The total number of τ_m data points is > 60,000 for each experimental condition.

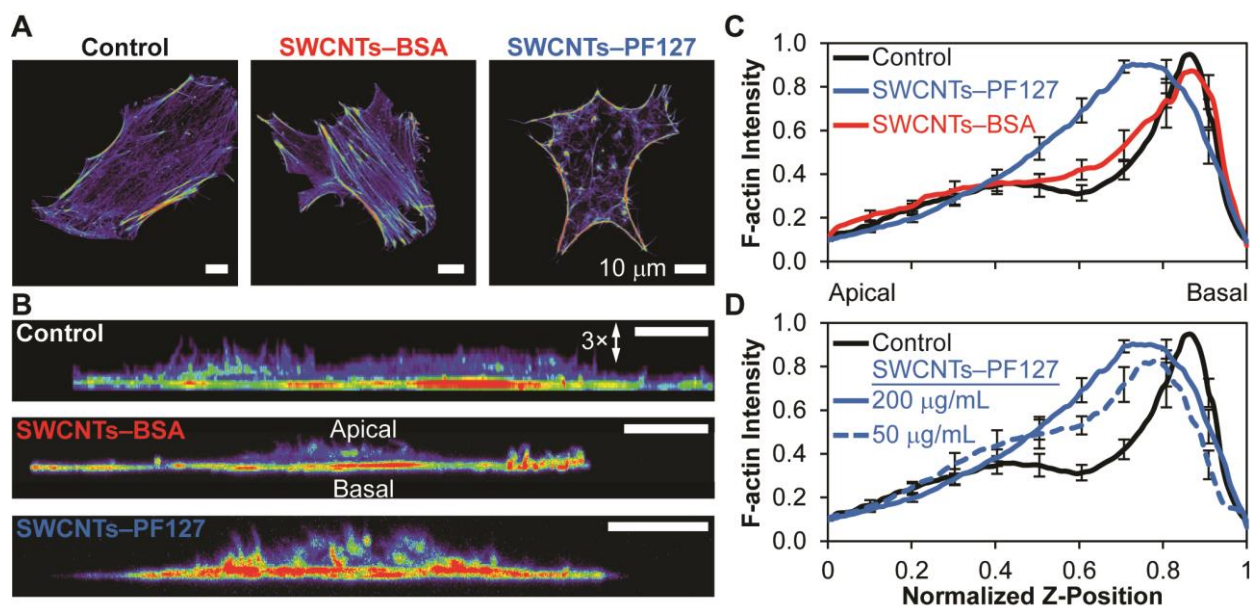


Fig. 4 Cells exposed to SWCNTs–PF127 but not SWCNTs–BSA possessed redistributed F-actin structures. Confocal Z-stack heat maps of the fluorescence intensity of Oregon Green 488 phalloidin that labeled F-actin of individual HeLa cells (A) compressed in Z or (B) compressed in Y showed altered F-actin structures with cellular exposure to SWCNTs–PF127. Note that the control image is stretched by 3× in the Z-direction to enable easier visualization. (C) Quantification of the confocal X–Z heat maps compressed in Y from (B) show normalized F-actin intensity per pixel (Y-axis) versus normalized position within the cell (X-axis: 0 ≡ top or apical, 1 ≡ bottom or basal). Cellular exposure to 200 µg/mL of SWCNTs–BSA did not induce any changes in F-actin distribution relative to the control. (D) Cellular exposure to SWCNTs–PF127 caused an apical redistribution of F-actin structures in a dose-dependent manner. Error bars are standard error of the mean. $n = 4$ for control and $n \geq 6$ for all other conditions.

Although FLIM can be highly sensitive to numerous parameters and quenching does not necessarily indicate direct interactions, we have previously performed *in vitro* experiments that provided evidence that direct association of fluorescently labeled cellular compartments with SWCNTs, instead of secondary effects from SWCNT exposure, resulted in the fluorescence lifetime quenching.⁵² Also, the fluorophore component of GFP is somewhat shielded from the environment outside of the protein structure, minimizing changes in fluorescent lifetime that would have arisen simply due to slight but not meaningful changes in protein environment.⁶⁸ Indeed, FLIM of fluorescence lifetime of fluorescent proteins has been successfully used to indicate cellular stress,⁷⁷ events associated with apoptosis⁷⁸ and differing membrane environments.⁷⁹

SWCNTs–PF127 redistribute F-actin inside cells

Because we found a preferential association of SWCNTs–PF127 with F-actin but not for SWCNTs–BSA, we next examined if SWCNTs–PF127 affected the structural organization of F-actin compared with SWCNTs–BSA. We labelled F-actin with Oregon Green 488 phalloidin for more complete visualization and collected numerous series of confocal images along the vertical direction, hereafter referred to as Z-stacks, and then compressed them along the Y- or Z-direction to identify any re-organization of F-actin after cellular exposure to SWCNTs–PF127 or SWCNTs–BSA. Control cells possessed typical stress fibers and cortical F-actin structures⁸⁰ (Fig. 4A,B and Fig. S5A,B). Cells exposed to 200 µg/mL of SWCNTs–PF127 for 24 h possessed dramatically altered F-actin structures, yet the F-actin distribution within cells exposed to SWCNTs–BSA was similar to control. Quantification of the fluorescence intensity per pixel of Oregon Green 488 phalloidin that labeled F-actin along the Z-direction of the X–Z confocal images compressed in Y showed that

F-actin in control cells had the largest intensity at the basal cellular regions while the rest of the cell possessed weaker intensity except for a slight increase for the actin cap⁸¹ at ~0.4 of the normalized Z-position (Fig. 4C and Fig. S5C,D). F-actin within cells exposed to SWCNTs–PF127 was redistributed toward the apical surface (Fig. 4C) in an exposure dose-dependent manner (Fig. 4D), yet cells exposed to SWCNTs–BSA did not have an altered distribution of F-actin structures, even for an exposure of 200 µg/mL, the highest exposure dose investigated.

SWCNTs–BSA redistribute endosomes inside cells

Since HeLa cells that were exposed to SWCNTs–BSA showed a significantly quenched average τ_m of GFP-RhoB GTPase that labeled endosomes compared to cells exposed to SWCNTs–PF127, we investigated the number and distribution of endosomes using confocal fluorescence microscopy of GFP-RhoB GTPase. To estimate the number of endosomes per cell, we quantified the number of endosomes discernable from the X–Y confocal images compressed in Z (Fig. 5A and Fig. S6A) using basic image processing methods to minimize bias. Control HeLa cells possessed 114 ± 18 endosomes, and 24 h of continuous cellular exposure to 50 µg/mL of SWCNTs–PF127 did not significantly alter endosome number (Fig. 5B and Fig. S6C). However, cells exposed to 50 µg/mL of SWCNTs–BSA possessed a significant increase in the number of endosomes per cell.

To determine if cellular exposure to SWCNTs–BSA altered endosome distribution, we analyzed X–Z images compressed in Y of endosomes (Fig. 5C and Fig. S6B). Quantification of the fluorescence intensity per pixel of GFP-RhoB GTPase along the Z-direction showed that control cells and cells exposed to SWCNTs–PF127 had similar endosomal distributions, but cells exposed to SWCNTs–BSA

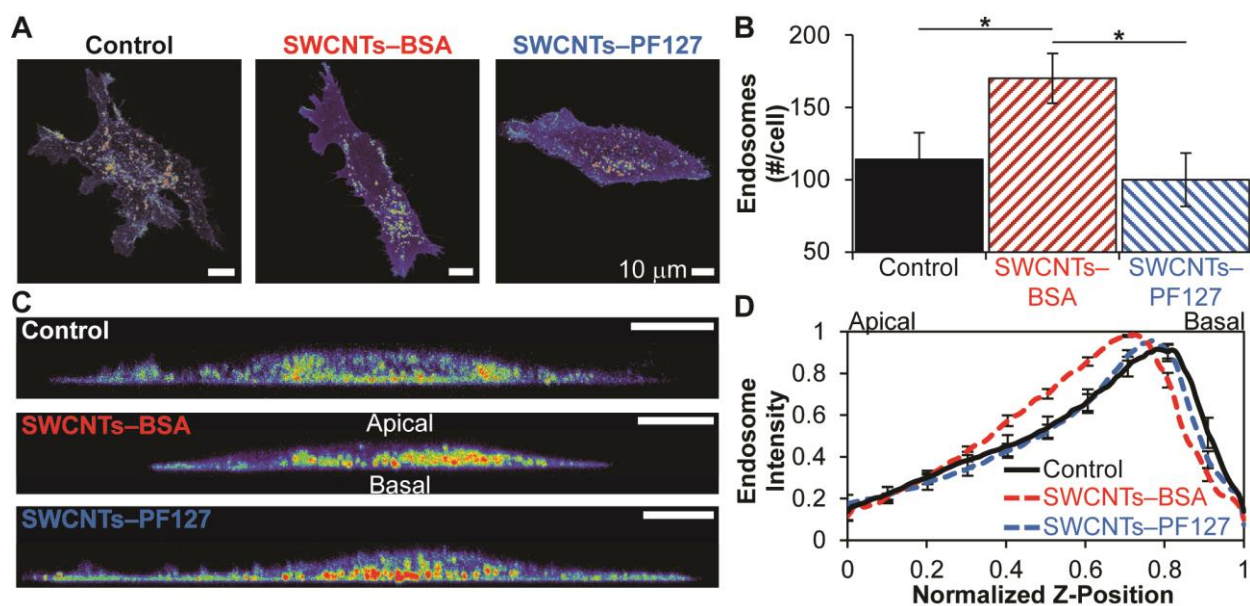


Fig. 5 24 h of continuous cellular exposure to SWCNTs-BSA but not SWCNTs-PF127 increased the number and localization of endosomes. (A) Confocal X-Y heat maps compressed in the Z-direction of the fluorescence intensity of GFP-RhoB GTPase that labeled endosomes of individual HeLa cells. (B) After 24 h of continuous exposure to 50 $\mu\text{g}/\text{mL}$ of SWCNTs-BSA or SWCNTs-PF127, there were statistically more endosomes within cells exposed to SWCNTs-BSA than within control cells or cells exposed to SWCNTs-PF127. (C) Confocal X-Z heat maps compressed in Y showed a slightly altered distribution for cells exposed to SWCNTs-BSA. (D) Cells exposed to SWCNTs-BSA possessed a more apical distribution of fluorescence intensity from GFP RhoB GTPase that labeled endosomes compared to control cells or cells exposed to SWCNTs-PF127. $n \geq 8$, error bars are standard error of the mean, and * indicates $p < 0.05$.

had a slight apical shift in endosome fluorescence intensity (Fig. 5D and Fig. S6D). While our measurement of endosomes was unable to distinguish subtle differences between early and late endosome states and was performed after 24 h of continuous exposure to SWCNTs, we were able to determine the long-term effects of SWCNTs on endosomes and sub-cellular trafficking which has broad implications for the utilization of SWCNTs in biomedical applications such as sub-cellular sensing, drug and nucleic acid delivery and use as an immunoadjuvant.

SWCNTs-BSA redistribute ER and vesicles inside cells

Since the endocytic pathway may ultimately result in material localization near the ER, 24 h of cellular exposure to SWCNTs-BSA

increased endosomes and SWCNTs-BSA co-registered with ER and vesicles, we hypothesized that SWCNTs-BSA would also alter ER and vesicle sub-cellular localization. Therefore, we performed confocal and widefield fluorescence imaging to determine the three-dimensional localization of ER and vesicles and to quantify their relative abundance per cell. Control cells possessed perinuclear fluorescence intensity from FM 4-64 that labeled ER and vesicles (Fig. 6A and Fig. S7A). Cells exposed to 50 $\mu\text{g}/\text{mL}$ of SWCNTs-PF127 possessed similar distributions compared to control cells, but cells exposed to 50 $\mu\text{g}/\text{mL}$ of SWCNTs-BSA had significant differences in the sub-cellular organization of ER and vesicles, resulting in increased fluorescence intensity of FM 4-64 that labeled ER and vesicles per cell (Fig. 6B and Supporting Information Fig. 5C)

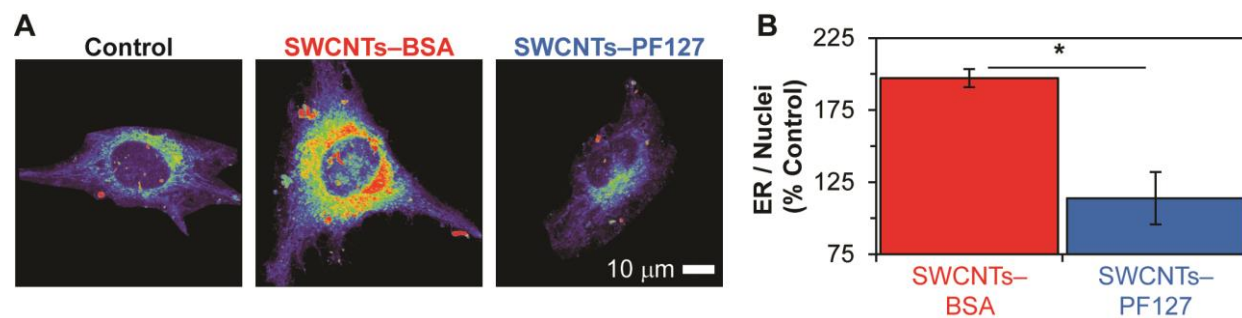


Fig. 6 Cellular exposure to SWCNTs-BSA but not SWCNTs-PF127 altered the fluorescence localization and intensity of FM 4-64 that labeled ER and vesicles. (A) Confocal X-Y fluorescence heat maps compressed in Z of FM 4-64 that labeled ER and vesicles showed perinuclear sub-cellular localizations but higher overall fluorescence intensity and distribution around the nucleus for cells exposed to SWCNTs-BSA. (B) Quantification from widefield images of the fluorescence intensity of FM 4-64 divided by the fluorescence intensity of DAPI that labeled the DNA of HeLa cell nuclei and normalized to control showed that the intensity of FM 4-64 that labeled ER and vesicles was statistically increased for cells exposed to SWCNTs-BSA but not for cells exposed to SWCNTs-PF127. The * indicates statistical significance ($p < 0.05$), the error bars are standard error of the mean and $n > 20$ fields of view for the widefield results.

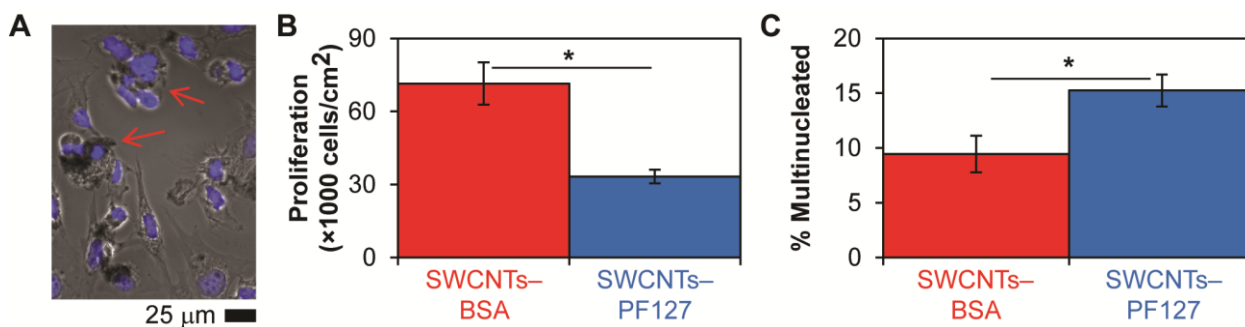


Fig. 7 Downstream impacts of differential SWCNT treatment. (A) Representative image of HeLa cells exposed to 200 $\mu\text{g}/\text{mL}$ of SWCNTs-PF127. Exposure to SWCNTs-PF127 reduced cellular proliferation and increased multi-nucleation (arrows). (B) Quantification of the reduction of cellular proliferation for a cellular exposure to 200 $\mu\text{g}/\text{mL}$ of SWCNTs-PF127 or SWCNTs-BSA. Cells exposed to SWCNTs-BSA possessed similar proliferation compared to control. (C) Quantification of multi-nucleation events per cell when exposed to 200 $\mu\text{g}/\text{mL}$ of SWCNTs. Lines with * indicate statistical significance ($p < 0.05$), error bars are standard error of the mean and $n > 600$ cells.

and altered X-Z distribution (Fig. S7B,D). As real-space imaging showed co-registration of SWCNTs-BSA but not SWCNTs-PF127 with ER and vesicles, these results demonstrated that the presence of SWCNTs-BSA with ER and vesicles led to the observed cellular alterations.

Downstream impacts of differential SWCNT treatment

Redistribution of different sub-cellular compartments results in downstream impacts on cellular function.^{82,83} To show the consequences of differential sub-cellular processing resulting from differential SWCNT dispersing agents, we quantified the downstream impacts of F-actin reorganization induced by cellular exposure to SWCNTs-PF127 and metabolic vesicular processing from cellular exposure to SWCNTs-BSA. Cellular exposure to SWCNTs-PF127 resulted in division defects and multi-nucleation associated with F-actin dependent processes, such as cytokinesis, but these were not present or present to a much lesser degree in cells exposed to SWCNTs-BSA (Fig. 7A and Fig. S8A,C). At the standard cellular seeding density and a 200 $\mu\text{g}/\text{mL}$ SWCNT exposure, cells exposed to SWCNTs-PF127 showed an $\sim 50\%$ reduction in cellular proliferation (Fig. 7B) and an $\sim 60\%$ increase in multi-nucleation (Fig. 7C and Fig. S8B) compared to cells exposed to SWCNTs-BSA.

Dispersing agent interfacial properties, endosome escape and differential sub-cellular trafficking

As the SWCNT interface, the dispersing agent should play an important role in the cellular processing of SWCNTs,⁸⁴ and previous studies with other nanocarbon materials have shown that protein coatings affect cellular uptake and toxicity.^{85,86} We have shown here that SWCNTs-PF127 co-registers with and alters apical F-actin structures, while SWCNTs-BSA co-registers with and alters ER and vesicles. PF127 is membrane active,^{87,88} and SWCNTs dispersed with PF127 can incorporate into cellular membranes without penetrating the bilayer.³¹ Drawing insight from these results and knowledge, we hypothesized that the membrane activity of PF127 facilitates destabilization of endosomes resulting in endosome rupture and escape, releasing internalized SWCNTs-PF127 into the apical regions of the cell, enabling SWCNTs-PF127 to directly interact with apical F-actin structures. Conversely, BSA does not facilitate endosome escape, and SWCNTs-BSA proceed through the endocytic pathway, ultimately being deposited in vesicles and around the ER.

To test this hypothesis, we designed an experiment to determine if a similar sub-cellular localization to cells exposed to SWCNTs-PF127 could be obtained by destabilizing endosomes during a cellular exposure to SWCNTs-BSA. To enable endosome escape, we exposed cells to chloroquine (see Methods) which is a known endosome disrupter that has been used to safely enhance transfection efficiency.^{60,89-93} Cells were exposed to both SWCNTs-BSA and chloroquine for 4 h and were either immediately fixed, referred to as 0 h post exposure, or had their media exchanged for fresh, complete cell culture media and allowed to incubate for 15 h, referred to as 15 h post exposure.

Cellular exposure to chloroquine resulted in no grossly observable effects on cellular vitality. Cellular exposure to chloroquine had little effect on the sub-cellular localization or fluorescence intensities of FM 4-64 that labeled ER and vesicles or Oregon Green 488 phalloidin that labeled F-actin for cells exposed to SWCNTs-PF127 (Fig. 8B and Fig. S9). These lacks of changes indicate that the additional exposure of chloroquine to cells exposed to SWCNTs-PF127 did not have any substantial effect since PF127 already destabilized endosomes.

For cells exposed to SWCNTs-BSA and chloroquine with 0 h post exposure, F-actin structures and the distribution of ER and vesicles were similar to cells exposed to SWCNTs-BSA without chloroquine. However, after 15 h post exposure from SWCNTs-BSA and chloroquine, we observed dramatic alterations to the sub-cellular compartments that mimicked those of cells exposed to SWCNTs-PF127 (Fig. 8 and Fig. S9). The fluorescence intensity of Oregon Green 488 phalloidin that labeled F-actin increased to levels similar to that of cells exposed to SWCNTs-PF127. At the same time, the fluorescence intensity of FM 4-64 that labeled ER and vesicles was reduced to levels similar to that of cells exposed to SWCNTs-PF127. However, we note that although these sub-cellular fluorescence intensities changed, we did not observe a significant apical redistribution of F-actin structures for cells exposed to SWCNTs-BSA and chloroquine after 15 h post exposure compared to chloroquine treatment alone.

This data demonstrates that by inducing endosome disruption through cellular exposure to chloroquine, the sub-cellular of trafficking of SWCNTs-BSA was changed. Instead of remaining in the endocytic pathway and increasing the fluorescence intensity of FM 4-64 that labeled ER and vesicles, SWCNTs-BSA was released from endosomes, enabling interactions with F-actin structures, in a similar manner to cells exposed to SWCNTs-PF127 without

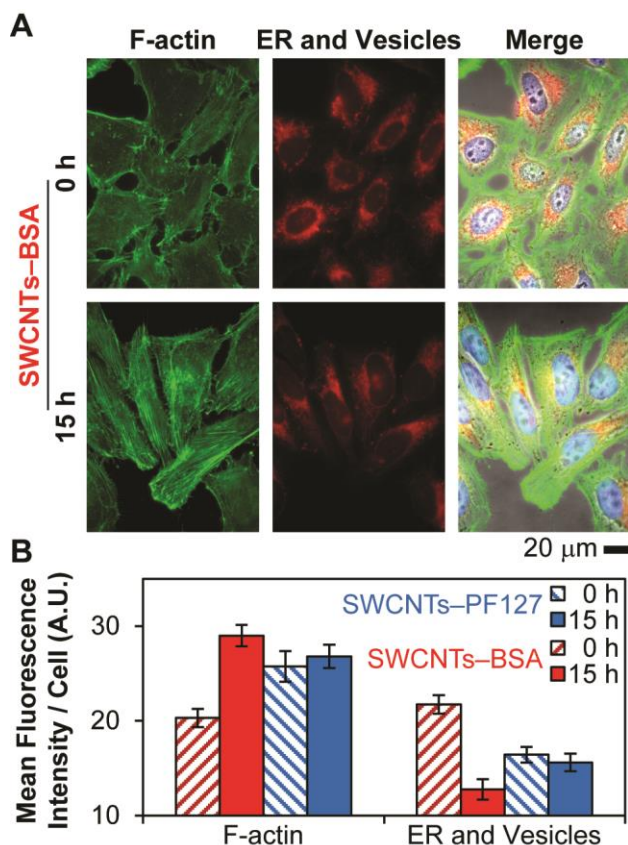


Fig. 8 Differential sub-cellular trafficking of SWCNTs *via* disruption of endosomes. (A) HeLa cells that were exposed to SWCNTs–BSA and chloroquine, an endosome disrupter, and then either immediately fixed, 0 h, or were given fresh, complete cell culture media for 15 h showed a time-dependent alteration to F-actin structures that ultimately was similar to that of cells exposed to SWCNTs–PF127. For instance, after 15 h post exposure, there were more intracellular stress fibers compared to primarily only cortical (peripheral) F-actin at 0 h post exposure. (B) Quantification of the fluorescence intensity of Oregon Green 488 phalloidin that labeled F-actin and the fluorescence intensity of FM 4-64 that labeled ER and vesicles demonstrated that the sub-cellular processing of SWCNTs–BSA was altered by cellular exposure to chloroquine, ultimately after 15 h post exposure mimicking that of cells exposed to SWCNTs–PF127. Cellular exposure to chloroquine had minimal effects on cells exposed to SWCNTs–PF127. Error bars are standard error of the mean. $n = 10$ fields of view.

chloroquine. We interpret these results to indicate that the dispersing agent PF127 facilitates endosome destabilization, allowing for SWCNTs–PF127 to interact with apical F-actin structures. Furthermore, since SWCNTs–BSA also interacted with F-actin structures upon liberation from the endocytic pathway, it experimentally suggested that SWCNTs might have an energetically favorable interaction with F-actin, as predicted by modeling.^{52,94}

Conclusions

Non-covalent dispersions of SWCNTs can be trafficked to different sub-cellular compartments based on SWCNT coating. Cellular exposure to SWCNTs–BSA for 24 h resulted in co-

registration of SWCNTs–BSA with ER and vesicles, an increase in the number and apical distribution of endosomes per cell, and an alteration of the sub-cellular distribution of FM 4-64 that labeled ER and vesicles. In contrast, cellular exposure to SWCNTs–PF127 resulted in co-registration of SWCNTs–PF127 with apical F-actin structures and alterations to the sub-cellular distribution of F-actin structures. Interestingly, chloroquine, an endosome disrupter, enabled SWCNTs–BSA to escape endosomes and interact with apical F-actin, leading to an alteration of F-actin structures that was similar to alterations induced by SWCNTs–PF127 alone. Therefore, these results indicate a design parameter for non-covalent modifications of SWCNTs to target sub-cellular pathways for biomedical applications such as sub-cellular sensing, bioactive molecule delivery and use as an immunoadjuvant, while preserving the intrinsic, attractive properties and structure of SWCNTs.

Acknowledgements

We thank Lance Davidson for providing GFP-moesin and P. D. Boyer for useful discussion. This work was supported by the National Science Foundation through grants CMMI-1335417 (M.F.I.), CBET-0954421 (K.N.D.) and CMMI-1300476 (K.N.D.).

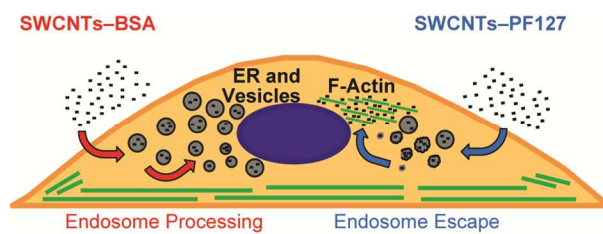
Notes and references

1. A. Bianco, K. Kostarelos and M. Prato, *Chem. Commun.*, 2011, **47**, 10182-10188.
2. A. Battigelli, C. Ménard-Moyon, T. D. Ros, M. Prato and A. Bianco, *Adv. Drug Delivery Rev.*, 2013, **65**, 1899-1920.
3. Z. Liu, S. M. Tabakman, Z. Chen and H. Dai, *Nat. Protoc.*, 2009, **4**, 1372-1381.
4. L. A. Girifalco, M. Hodak and R. S. Lee, *Phys. Rev. B: Condens. Matter Mater. Phys.*, 2000, **62**, 13104-13110.
5. D. X. Cui, F. R. Tian, C. S. Ozkan, M. Wang and H. J. Gao, *Toxicol. Lett.*, 2005, **155**, 73-85.
6. J.-P. Kaiser, P. Wick, P. Manser, P. Spohn and A. Bruinink, *J. Mater. Sci.: Mater. Med.*, 2008, **19**, 1523-1527.
7. D. Liu, C. Yi, D. Zhang, J. Zhang and M. Yang, *ACS Nano*, 2010, **4**, 2185-2195.
8. K. Luoto, M. Holopainen, M. Perander, K. Karppinen and K. M. Savolainen, *Cent. Eur. J. Public Health*, 1996, **4**, Suppl:29-32.
9. B. D. Holt, P. A. Short, A. D. Rape, Y. L. Wang, M. F. Islam and K. N. Dahl, *ACS Nano*, 2010, **4**, 4872-4878.
10. Z. Liu, J. T. Robinson, S. M. Tabakman, K. Yang and H. Dai, *Mater. Today*, 2011, **14**, 316-323.
11. W. Wenseleers, I. I. Vlasov, E. Goovaerts, E. D. Obraztsova, A. S. Lobach and A. Bouwen, *Adv. Funct. Mater.*, 2004, **14**, 1105-1112.
12. M. F. Islam, E. Rojas, D. M. Bergey, A. T. Johnson and A. G. Yodh, *Nano Lett.*, 2003, **3**, 269-273.
13. L. Mrowczynska and J. Bielawski, *Cell. Mol. Biol. Lett.*, 2001, **6**, 881-895.
14. B. P. Ross, A. C. Braddy, R. P. McGeary, J. T. Blanchfield, L. Prokai and I. Toth, *Mol. Pharm.*, 2004, **1**, 233-245.
15. B. D. Holt, K. N. Dahl and M. F. Islam, *Small*, 2011, **7**, 2348-2355.
16. B. D. Holt, M. C. McCorry, P. D. Boyer, K. N. Dahl and M. F. Islam, *Nanoscale*, 2012, **4**, 7425-7434.

17. X. Dang, H. Yi, M.-H. Ham, J. Qi, D. S. Yun, R. Ladewski, M. S. Strano, P. T. Hammond and A. M. Belcher, *Nat. Nanotechnol.*, 2011, **6**, 377-384.
18. E. Heister, E. W. Brunner, G. R. Dieckmann, I. Jurewicz and A. B. Dalton, *ACS Appl. Mater. Interfaces*, 2013, **5**, 1870-1891.
19. N. W. S. Kam and H. J. Dai, *J. Am. Chem. Soc.*, 2005, **127**, 6021-6026.
20. M. Zheng, A. Jagota, E. D. Semke, B. A. Diner, R. S. McLean, S. R. Lustig, R. E. Richardson and N. G. Tassi, *Nat. Mater.*, 2003, **2**, 338-342.
21. P. Bilalis, D. Katsigiannopoulos, A. Avgeropoulos and G. Sakellariou, *RSC Adv.*, 2014, **4**, 2911-2934.
22. N. W. S. Kam, T. C. Jessop, P. A. Wender and H. J. Dai, *J. Am. Chem. Soc.*, 2004, **126**, 6850-6851.
23. N. W. S. Kam, Z. A. Liu and H. J. Dai, *Angew. Chem., Int. Ed.*, 2006, **45**, 577-581.
24. N. W. S. Kam, M. O'Connell, J. A. Wisdom and H. J. Dai, *Proc. Natl. Acad. Sci. U. S. A.*, 2005, **102**, 11600-11605.
25. Q. Wan, M. Liu, J. Tian, F. Deng, G. Zeng, Z. Li, K. Wang, Q. Zhang, X. Zhang and Y. Wei, *Polym. Chem.*, 2015, **6**, 1786-1792.
26. Q. Wan, J. Tian, M. Liu, G. Zeng, Z. Li, K. Wang, Q. Zhang, F. Deng, X. Zhang and Y. Wei, *RSC Adv.*, 2015, **5**, 25329-25336.
27. G. Sahay, D. Y. Alakhova and A. V. Kabanov, *J. Controlled Release*, 2010, **145**, 182-195.
28. E. L. Bakota, L. Aulisa, D. A. Tsyboulski, R. B. Weisman and J. D. Hartgerink, *Biomacromolecules*, 2009, **10**, 2201-2206.
29. D. Pantarotto, C. D. Partidos, R. Graff, J. Hoebeke, J.-P. Briand, M. Prato and A. Bianco, *J. Am. Chem. Soc.*, 2003, **125**, 6160-6164.
30. E. Venturelli, C. Fabbro, O. Chaloin, C. Ménard-Moyon, C. R. Smulski, T. Da Ros, K. Kostarelos, M. Prato and A. Bianco, *Small*, 2011, **7**, 2179-2187.
31. P. Yaron, B. Holt, P. Short, M. Losche, M. Islam and K. Dahl, *J. Nanobiotechnol.*, 2011, **9**, 45(01):45(15).
32. E. Andreoli, R. Suzuki, A. W. Orbaek, M. S. Bhutani, R. H. Hauge, W. Adams, J. B. Fleming and A. R. Barron, *J. Mater. Chem. B*, 2014, **2**, 4740-4747.
33. J. Cheng, K. A. S. Fernando, L. M. Veca, Y.-P. Sun, A. I. Lamond, Y. W. Lam and S. H. Cheng, *ACS Nano*, 2008, **2**, 2085-2094.
34. D. Pantarotto, J.-P. Briand, M. Prato and A. Bianco, *Chem. Commun.*, 2004, 16-17.
35. M. Raoof, Y. Mackeyev, M. A. Cheney, L. J. Wilson and S. A. Curley, *Biomaterials*, 2012, **33**, 2952-2960.
36. A. Battigelli, J. Russier, E. Venturelli, C. Fabbro, V. Petronilli, P. Bernardi, T. Da Ros, M. Prato and A. Bianco, *Nanoscale*, 2013, **5**, 9110-9117.
37. S. L. Yoong, B. S. Wong, Q. L. Zhou, C. F. Chin, J. Li, T. Venkatesan, H. K. Ho, V. Yu, W. H. Ang and G. Pastorin, *Biomaterials*, 2014, **35**, 748-759.
38. F. Zhou, S. Wu, B. Wu, W. R. Chen and D. Xing, *Small*, 2011, **7**, 2727-2735.
39. F. Zhou, S. Wu, Y. Yuan, W. R. Chen and D. Xing, *Small*, 2012, **8**, 1543-1550.
40. F. F. Zhou, D. Xing, B. Y. Wu, S. N. Wu, Z. M. Ou and W. R. Chen, *Nano Lett.*, 2010, **10**, 1677-1681.
41. K. Kostarelos, L. Lacerda, G. Pastorin, W. Wu, S. Wieckowski, J. Luangsivilay, S. Godefroy, D. Pantarotto, J. P. Briand, S. Muller, M. Prato and A. Bianco, *Nat. Nanotechnol.*, 2007, **2**, 108-113.
42. B. D. Holt, K. N. Dahl and M. F. Islam, *ACS Nano*, 2012, **6**, 3481-3490.
43. P. D. Boyer, B. D. Holt, M. F. Islam and K. N. Dahl, *Soft Matter*, 2013, **9**, 758-764.
44. M. C. Hersam, *Nat. Nanotechnol.*, 2008, **3**, 387-394.
45. M. J. O'Connell, S. M. Bachilo, C. B. Huffman, V. C. Moore, M. S. Strano, E. H. Haroz, K. L. Rialon, P. J. Boul, W. H. Noon, C. Kittrell, J. P. Ma, R. H. Hauge, R. B. Weisman and R. E. Smalley, *Science*, 2002, **297**, 593-596.
46. G. K. M. Mutlu, G. R. S. Budinger, A. A. Green, D. Urlich, S. Soberanes, S. E. Chiarella, G. F. Alheid, D. R. McCrimmon, I. Szleifer and M. C. Hersam, *Nano Lett.*, 2010, **10**, 1664-1670.
47. R. B. Weisman, *Anal. Bioanal. Chem.*, 2010, **396**, 1015-1023.
48. H. Kataura, Y. Kumazawa, Y. Maniwa, I. Umezumi, S. Suzuki, Y. Ohtsuka and Y. Achiba, *Synth. Met.*, 1999, **103**, 2555-2558.
49. M. S. Dresselhaus and G. E. Dresselhaus, P. C., *Science of Fullerenes and Carbon Nanotubes*, Academic Press, San Diego, 1996.
50. S. M. Bachilo, M. S. Strano, C. Kittrell, R. H. Hauge, R. E. Smalley and R. B. Weisman, *Science*, 2002, **298**, 2361-2366.
51. R. B. Weisman and S. M. Bachilo, *Nano Lett.*, 2003, **3**, 1235-1238.
52. B. D. Holt, H. Shams, T. A. Horst, S. Basu, A. D. Rape, Y.-L. Wang, G. K. Rohde, M. R. K. Mofrad, M. F. Islam and K. N. Dahl, *J. Funct. Biomater.*, 2012, **3**, 398-417.
53. M. F. Islam, D. E. Milkie, O. N. Torrens, A. G. Yodh and J. M. Kikkawa, *Phys. Rev. B: Condens. Matter Mater. Phys.*, 2005, **71**, 201401(R).
54. D. E. Johnston, M. F. Islam, A. G. Yodh and A. T. Johnson, *Nat. Mater.*, 2005, **4**, 589-592.
55. M. S. Arnold, A. A. Green, J. F. Hulvat, S. I. Stupp and M. C. Hersam, *Nat. Nanotechnol.*, 2006, **1**, 60-65.
56. M. L. Becker, J. A. Fagan, N. D. Gallant, B. J. Bauer, V. Bajpai, E. K. Hobbie, S. H. Lacerda, K. B. Migler and J. P. Jakupciak, *Adv. Mater.*, 2007, **19**, 939-945.
57. J. A. Fagan, M. L. Becker, J. Chun and E. K. Hobbie, *Adv. Mater.*, 2008, **20**, 1609-1613.
58. Y. Y. Huang, T. P. J. Knowles and E. M. Terentjev, *Adv. Mater.*, 2009, **21**, 3945-3948.
59. P. Litman, M. Amieva and H. Furthmayr, *BMC Cell Biol.*, 2000, **1**, 1(1)-1(9).
60. T. Shiraiishi and P. E. Nielsen, *Nat. Protocols*, 2006, **1**, 633-636.
61. M. S. Dresselhaus, G. Dresselhaus, R. Saito and A. Jorio, *Phys. Rep.*, 2005, **409**, 47-99.
62. M. S. Dresselhaus and P. C. Eklund, *Adv. Phys.*, 2000, **49**, 705-814.
63. D. A. Heller, S. Baik, T. E. Eurell and M. S. Strano, *Adv. Mater.*, 2005, **17**, 2793-2799.
64. J. W. Kang, F. T. Nguyen, N. Lue, R. R. Dasari and D. A. Heller, *Nano Lett.*, 2012, **12**, 6170-6174.
65. W. Becker, *The bh TCSPC Handbook*, Third edn., 2008.
66. R. R. Duncan, A. Bergmann, M. A. Cousin, D. K. Apps and M. J. Shipston, *J. Microsc.*, 2004, **215**, 1-12.
67. M. Köllner and J. Wolfrum, *Chem. Phys. Lett.*, 1992, **200**, 199-204.
68. M. Y. Berezin and S. Achilefu, *Chem. Rev.*, 2010, **110**, 2641-2684.
69. P. Cherukuri, C. J. Gannon, T. K. Leeuw, H. K. Schmidt, R. E. Smalley, S. A. Curley and R. B. Weisman, *Proc. Natl. Acad. Sci. U. S. A.*, 2006, **103**, 18882-18886.
70. H. Jin, D. A. Heller and M. S. Strano, *Nano Lett.*, 2008, **8**, 1577-1585.
71. D. A. Tsyboulski, S. M. Bachilo and R. B. Weisman, *Nano Lett.*, 2005, **5**, 975-979.
72. K. Welscher, S. P. Sherlock and H. Dai, *Proc. Natl. Acad. Sci. U. S. A.*, 2011, **108**, 8943-8948.

73. D. A. Heller, P. W. Barone, J. P. Swanson, R. M. Mayrhofer and M. S. Strano, *J. Phys. Chem. B*, 2004, **108**, 6905-6909.
74. Z. Liu, S. Tabakman, S. Sherlock, X. L. Li, Z. Chen, K. L. Jiang, S. S. Fan and H. J. Dai, *Nano Res.*, 2010, **3**, 222-233.
75. Z. A. Liu, X. L. Li, S. M. Tabakman, K. L. Jiang, S. S. Fan and H. J. Dai, *J. Am. Chem. Soc.*, 2008, **130**, 13540-13541.
76. H. Jin, D. A. Heller, R. Sharma and M. S. Strano, *ACS Nano*, 2009, **3**, 149-158.
77. T. Nakabayashi, I. Nagao, M. Kinjo, Y. Aoki, M. Tanaka and N. Ohta, *Photochem. Photobiol. Sci.*, 2008, **7**, 671-674.
78. T. Ito, S. Oshita, T. Nakabayashi, F. Sun, M. Kinjo and N. Ohta, *Photochem. Photobiol. Sci.*, 2009, **8**, 763-767.
79. B. Treanor, P. M. P. Lanigan, K. Suhling, T. Schreiber, I. Munro, M. A. A. Neil, D. Phillips, D. M. Davis and P. M. W. French, *J. Microsc.*, 2005, **217**, 36-43.
80. T. D. Pollard and W. C. Earnshaw, *Cell Biology*, Elsevier Inc., Second edn., 2008.
81. S. B. Khatau, C. M. Hale, P. J. Stewart-Hutchinson, M. S. Patel, C. L. Stewart, P. C. Searson, D. Hodzic and D. Wirtz, *Proc. Natl. Acad. Sci. U. S. A.*, 2009, **106**, 19017-19022.
82. P. A. Janmey and C. Chaponnier, *Curr. Opin. Cell Biol.*, 1995, **7**, 111-117.
83. G. J. Wang, J. G. Jackson and S. A. Thayer, *J. Neurochem.*, 2003, **87**, 85-94.
84. J. M. Anderson, *Annu. Rev. Mater. Res.*, 2001, **31**, 81-110.
85. X. Zhang, W. Hu, J. Li, L. Tao and Y. Wei, *Toxicol. Res.*, 2012, **1**, 62-68.
86. Y. Zhu, W. Li, Q. Li, Y. Li, Y. Li, X. Zhang and Q. Huang, *Carbon*, 2009, **47**, 1351-1358.
87. G. Dumortier, J. Grossiord, F. Agnely and J. Chaumeil, *Pharm. Res.*, 2006, **23**, 2709-2728.
88. G. Wu, H. A. Khant, W. Chiu and K. Y. C. Lee, *Soft Matter*, 2009, **5**, 1496-1503.
89. N. J. Caron, S. P. Quenneville and J. P. Tremblay, *Biochem. Biophys. Res. Commun.*, 2004, **319**, 12-20.
90. A. El-Sayed, S. Futaki and H. Harashima, *AAPS J.*, 2009, **11**, 13-22.
91. T. Katav, L. Liu, T. Traitel, R. Goldbart, M. Wolfson and J. Kost, *J. Controlled Release*, 2008, **130**, 183-191.
92. E. Jeon, H.-D. Kim and J.-S. Kim, *J. Biomed. Mater. Res., Part A*, 2003, **66A**, 854-859.
93. M. S. Wadhwa, D. L. Knoell, A. P. Young and K. G. Rice, *Bioconjugate Chem.*, 1995, **6**, 283-291.
94. H. Shams, B. D. Holt, S. H. Mahboobi, Z. Jahed, M. F. Islam, K. N. Dahl and M. R. K. Mofrad, *ACS Nano*, 2014, **8**, 188-197.

Table of contents entry



Real-space and fluorescence lifetime imaging reveal that non-covalently attached dispersing agents influence sub-cellular trafficking and localization of carbon nanotubes.